Geophys. J. R. astr. Soc. (1987) **91**, 667–691

Shock-induced temperatures of MgO

Bob Svendsen and Thomas J. Ahrens *Seismological Laboratory 252–21, California Institute of Technology, Pasadena, CA. 91125, USA*

Accepted 1987 April 23. Received 1987 April 20; in original form 1986 October 14

Summary. Shock-compressed MgO radiates thermally at temperatures between 2900 and 3700 K in the 170–200 GPa pressure range. A simple energy-transport model of the shocked-MgO-targets distinguishes between different shock-induced radiation sources in these targets and provides estimates of spectral absorption-coefficients, $a_{\lambda MgO}$, for shocked MgO (e.g. at 203 GPa, $a_{\lambda MgO} \sim 630$, 7500, 4200 and 3800 m^{-1}, at 450, 600, 750 and 900 nm, respectively). The experimentally inferred temperatures of the shock-compressed states of MgO are consistent with temperatures calculated for MgO assuming that (1) it deforms as an elastic fluid, (2) has a Dulong-Petit value for specific heat at constant volume in its shocked state, and (3) undergoes no phase transformation below 200 GPa.

Key words: shock compression, optical radiation, temperature, magnesium oxide

Introduction

The mechanical response of materials to high pressure has traditionally been investigated by shock wave or static compression experiments that constrain, among other things, the pressure–density 'equation-of-state' behaviour of these materials. As first demonstrated by Soviet workers (summarized by Kormer 1968), optical radiation from the shock-compressed state of transparent materials has the potential to constrain the temperature of the compressed state. The emission of radiation from shock-compressed transparent materials is rather remarkable from the point of view that these materials are, at least initially, dielectrics. Shock compression apparently transforms ionic materials (e.g. NaCl) into semiconductors (Kormer *et al.* 1966) with electrical conductivity up to 10^{10} times that of the uncompressed material. Among initially-covalent materials, Ahrens (1966) inferred a $\sim 10^2$ increase in the electrical conductivity of MgO shock-compressed above 92 GPa, and Knittle & Jeanloz (1986) inferred a similar increase in the electrical conductivity of FeO statically-compressed above 70 GPa. For MgO, at least, this change in electrical conductivity at high

pressure is thought likely to be due to extrinsic (e.g. defect) processes, rather than band-gap closure (e.g. Liberman 1978; Chang & Cohen 1984), as discussed below.

Oxides accepted as predominant chemical end-members of the material constituting the Earth's mantle include MgO, FeO, Al_2O_3, CaO and SiO_2. Of these, (Mg,Fe)O may be an actual constituent of the Earth's mantle below 670 km (e.g. Jeanloz & Thompson 1983). Hence the complete (P, T, ρ) equation-of-state of MgO is relevant to studies of the Earth's mantle. Among the mantle oxides, radiation emitted from SiO_2 (Lyzenga, Ahrens & Mitchell 1983) and CaO (Boslough, Ahrens & Mitchell 1984) shock-compressed above 60 and 140 GPa, respectively, has been studied using optical pyrometry (Kormer 1968; Lyzenga 1980). Optical radiation from MgO, Al_2O_3 and SiO_2, all shock-compressed to pressures below 75 GPa, has also been studied spectroscopically (Schmitt & Ahrens 1984; Schmitt, Svendsen & Ahrens 1986). If the wavelength-dependence of this radiation is consistent with a grey-body source, it may be interpreted in terms of the temperature and effective emissivity of the shock-compressed material. In the pressure range investigated, shock-induced radiation from both initially-amorphous SiO_2 (10 to 110 GPa) and initially crystalline (B1) CaO (140–180 GPa) is consistent with this type of source. Radiation from α-SiO_2, however, is clearly consistent with a greybody source only above 60 GPa (Lyzenga *et al.* 1983; Schmitt *et al.* 1986). Note that shock-compressed SiO_2 transforms to stishovite above 16 GPa and melts above 70 GPa (Lyzenga *et al.* 1983), while shock-compressed CaO transforms from a B1 to a B2 structure (Jeanloz *et al.* 1979), and FeO to an unidentified phase (e.g. Jeanloz & Ahrens 1980a; Jackson & Ringwood 1981), both above 70 GPa. Both MgO and Al_2O_3 apparently do not change phase during shock compression. Considering the sensitivity of optical radiation to energy processes, as well as the complexity of interpretation introduced by dynamic phase transformations (e.g. SiO_2: Lyzenga *et al.* 1983), we studied the thermo-mechanical response of shock-compressed MgO as a material apparently uncomplicated by phase transitions, at least below 200 GPa. Since the experimental results we present below are consistent with a simple classical (i.e. equilibrium) thermodynamic model of MgO, which includes the assumption of no phase transition, we conducted only 4 experiments.

Experimental

We conducted the experiments on a two-stage, light-gas gun (e.g. Jeanloz & Ahrens 1980a; Fig. 1). In these, a lexan-encased tantalum (Ta) flyer-plate, moving at 5.7–6.4 km s^{-1} (Table 6), impacted a 1.5 mm-thick Ta driver-plate in contact with the (100) face of a 3 mm-thick synthetic single-crystal of magnesium oxide (MgO: similar to those used by Vassiliou & Ahrens 1981). We covered the free-surface of the MgO crystal with an aluminium mask to avoid observing radiation from the target's edge. Radiation from the target reflects from a mirror, propagates through an objective lens, and is directed by a (dichroic) pellicle beam splitter and two half-silvered beam splitters into four detectors filtered at nominal wavelengths of 450, 600, 750 and 900 nm. We recorded the signal from each detector on a Tektronix 485 single-sweep oscilloscope and a LeCroy (model 8081) 100-MHz transient recorder.

Wanting to observe radiation from MgO, we attempted to minimize the radiation intensity of the Ta–MgO interface by vapour-depositing 500–1000 nm of silver (Ag) on MgO, and then placing the Ag 'film' in mechanical contact with the Ta driver-plate to form the target. Requiring a material that would not maintain a high temperature during the experiment, we chose Ag for its high thermal-conductivity at standard temperature and pressure (STP: 298 K and 0.1 MPa) and ease of deposition. We expected this Ag film to absorb any radiation from the Ta–Ag interface, heat up much less than a mechanical Ta–MgO interface (Urtiew & Grover 1974), and contain no trapped gas that could also contribute to interface radiation (Boslough 1985).

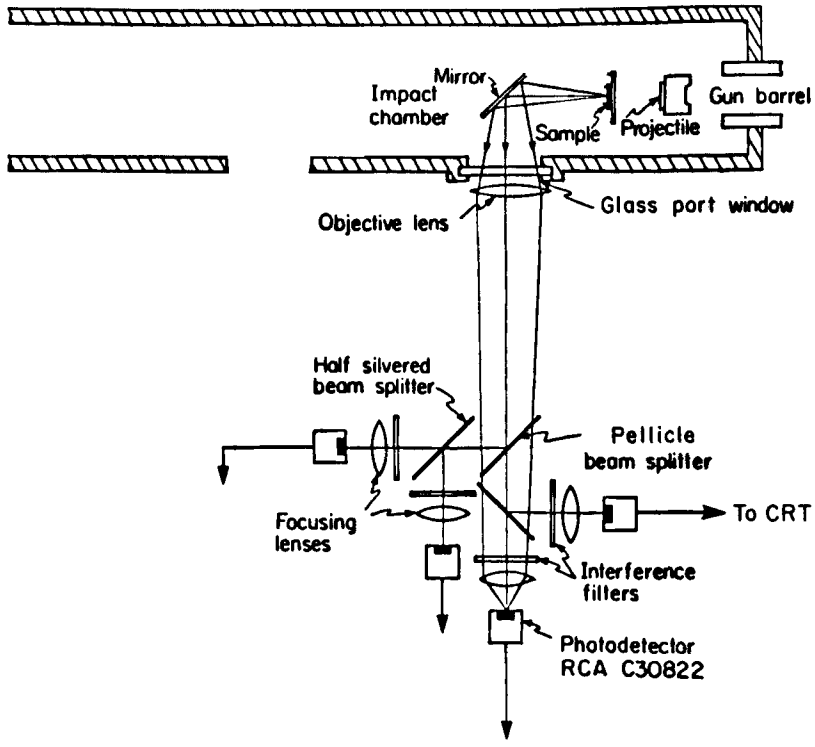

Figure 1. Geometry of the light-gas gun radiation experiment after Boslough (1984). The projectile, shot through the barrel, impacts the sample at velocities between 5.7 and 6.4 km s^{-1}. Radiation from the sample is bent 90° by the mirror, travels through the objective lens, and is divided up by the three beam-splitter arrangement among the four channels to the pyrometer. The resulting signals from the photodiode in each channel are monitored by oscilloscopes and LeCroy transient digital recorders.

Model calculations and data analysis

Our experiment begins when the projectile, containing the Ta flyer-plate, impacts the Ta driver-plate. This process generates two shock waves at the flyer–driver interface, one travelling forward into the driver plate and the other back into the projectile. When the shock wave propagating through the driver plate reaches the driver plate-film (Ta–Ag) interface, a lower-amplitude shock continues into the lower shock-impedance Ag-film, and a release wave is reflected back into the driver plate. Once the interface is compressed, the balance of mass and momentum require that the component of the material velocity and stress fields, respectively, in the driver plate and film normal to the interface be continuous across it. Consequently, the compressed state of the driver plate releases to a state having nearly the magnitude of the normal stress and material velocity of the shocked-Ag film. An analogous process occurs at the Ag–MgO interface, releasing the shock-compressed Ag to a state with essentially the same normal material velocity and stress as the shock-compressed MgO. Since the film is so thin, the driver plate releases (a second time) shortly after this to a similar state. Wave reverberations quickly bring the driver plate and film to states with the normal stress and material velocity of the shocked-MgO. All of this occurs on a time scale less than 1 nanosecond (ns), and is not detectable by the pyrometer.

The basic data is radiation intensity as a function of time at the four wavelengths mentioned above. Clearly, the time-resolution of the data is much better than the

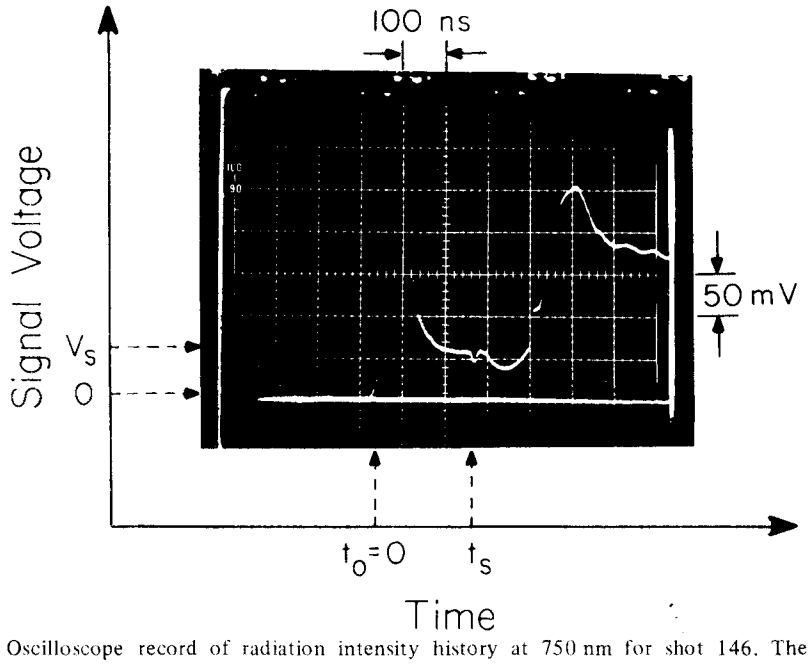

Figure 2. Oscilloscope record of radiation intensity history at 750 nm for shot 146. The radiation intensity rises sharply off-scale at $t = 0$ as the shock wave compresses the Ag-MgO interface to high temperature (see Table 2). Decay of the interface temperature and/or absorption of interface radiation in the growing shocked-MgO layer (see text) causes the observed intensity to decrease sharply with time to about 170 ns into the experiment, at which point the radiation intensity becomes approximately time-independent. After about 240 ns (t_s), the shock wave reaches the free surface of the MgO, and the experiment is over.

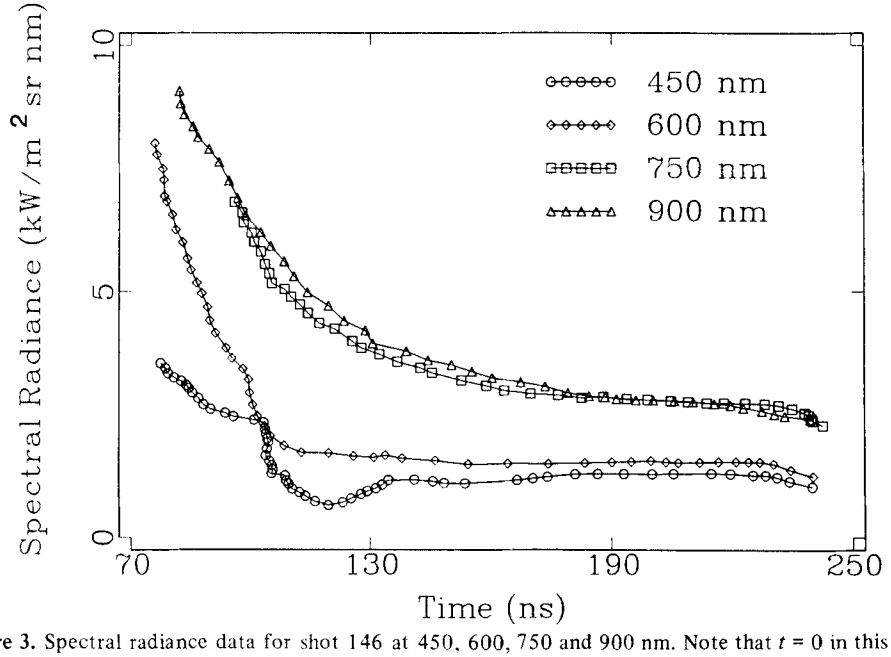

Figure 3. Spectral radiance data for shot 146 at 450, 600, 750 and 900 nm. Note that $t = 0$ in this figure has the same meaning as in Fig. 2.

wavelength-resolution. We present an example of these data in Fig. 2, an oscilloscope record at 750 nm for shot 146 (Table 6). Using the known radiation intensity of a standard lamp (Boslough 1984) at the observed wavelengths, we transform this raw data into experimental spectral radiation intensities (in the form of spectral radiance) as a function of time. The result of this procedure for shot 146 data is displayed in Fig. 3.

We interpret the temporal and wavelength variations of data in the context of the following model, a slight modification of Boslough's (1985) model (see also Boslough *et al.* 1986; Svendsen 1987). We assume that the shock-compressed/released Ag-film at the Ag–MgO interface, and shock-compressed MgO, are the only sources contributing to the observed radiation. Further, assume that the shocked-MgO layer radiates uniformly along the direction of shock propagation over the time scale of the observations. Then the total radiation intensity, $I_{\lambda \mathrm{mod}}(\lambda, t)$, a function of wavelength (λ), and time after the onset of radiation from the target, t, is the sum of that fraction of each source intensity that emerges from the front of the target, i.e.

$$I_{\lambda \mathrm{mod}}(\lambda, t) \equiv \hat{\epsilon}_{\lambda \mathrm{MgO}}(t)\, I_{\lambda \mathrm{pl}}(\lambda, T_{\mathrm{MgO}}) + \hat{\epsilon}_{\lambda \mathrm{INT}}(t)\, I_{\lambda \mathrm{pl}}[\lambda, T_{\mathrm{INT}}(t)], \tag{1}$$

where the λ subscript indicates a spectral quantity. In (1), T_{MgO} is the shock-compressed (Hugoniot) temperature of MgO (assumed homogeneous, uniform and constant), and $T_{\mathrm{INT}}(t)$ is the temperature of Ag at the Ag–MgO interface. Further,

$$\hat{\epsilon}_{\lambda \mathrm{MgO}}(t) \equiv [1 - r_{\lambda \mathrm{FS}}]\, \tau_{\lambda \mathrm{MgO,O}}(t)\, [1 - r_{\lambda \mathrm{SF}}]\, [1 + r_{\lambda \mathrm{INT}}\, \tau_{\lambda \mathrm{MgO}}(t)]\, [1 - \tau_{\lambda \mathrm{MgO}}(t)] \tag{2}$$

and

$$\hat{\epsilon}_{\lambda \mathrm{INT}}(t) \equiv [1 - r_{\lambda \mathrm{FS}}]\, \tau_{\lambda \mathrm{MgO,O}}(t)\, [1 - r_{\lambda \mathrm{SF}}]\, \tau_{\lambda \mathrm{MgO}}(t)\, [1 - r_{\lambda \mathrm{INT}}] \tag{3}$$

are the effective normal spectral emissivities of the shocked-MgO and Ag at the Ag–MgO interface, respectively, while $r_{\lambda \mathrm{FS}}$, $r_{\lambda \mathrm{SF}}$ and $r_{\lambda \mathrm{INT}}$ are the effective normal spectral reflectivities of the MgO free-surface, shock front and Ag–MgO interface, respectively. Also,

$$\tau_{\lambda \mathrm{MgO,O}}(t) \equiv \exp\, [-a^*_{\lambda \mathrm{MgO,O}}(1 - t/t_{\mathrm{exp}})] \tag{4}$$

and

$$\tau_{\lambda \mathrm{MgO}}(t) \equiv \exp\, [-a^*_{\lambda \mathrm{MgO}}\, t/t_{\mathrm{exp}}] \tag{5}$$

are the effective normal spectral transmissivities of unshocked and shocked-MgO layers, respectively. In (4) and (5), $a^*_{\lambda \mathrm{MgO,O}}$ and $a^*_{\lambda \mathrm{MgO}}$ are non-dimensional forms of the effective normal spectral coefficients of absorption in unshocked and shocked-MgO, respectively, given by

$$a^*_{\lambda \mathrm{MgO}} \equiv a_{\lambda \mathrm{MgO}}\, (U - v_{\mathrm{MgO}}) t_{\mathrm{exp}} \tag{6}$$

and

$$a^*_{\lambda \mathrm{MgO,O}} \equiv a_{\lambda \mathrm{MgO,O}}\, U t_{\mathrm{exp}}. \tag{7}$$

Note that $t_{\mathrm{exp}} \equiv d/U$ is the experimental time-scale, U is the shock-wave velocity in MgO, d is the initial thickness of the MgO layer in the target, and v_{MgO} is the material velocity of the shock-compressed state of MgO. Lastly, we have

$$I_{\lambda \mathrm{pl}}(\lambda, T) \equiv \frac{C_1}{\lambda^5\, [\exp\, (C_2/\lambda T) - 1]}$$

(with $C_1 \equiv 1.19088 \times 10^{-16}$ W · m^2 and $C_2 \equiv 1.4388 \times 10^{-2}$ m · K) as the Planck function.

Assuming the optical boundaries (e.g. Ag–MgO interface) are smooth (i.e. surface roughness much less than radiation wavelength), the effective normal spectral reflectivity of the boundary between any two of these layers is a function of the change in the (complex) index of refraction across the boundary (e.g. Siegel & Howell 1980: see below). The effective emissivities (2) and (3) are correct to first order in $r_{\lambda FS}$, $r_{\lambda SF}$ and $r_{\lambda INT}$; we assume second- and higher-order reflections are negligible (Boslough 1985; Svendsen 1987). Because of this approximation, (2) and (3) are, strictly speaking, lower bounds to $\hat{\epsilon}_{\lambda MgO}(t)$ and $\hat{\epsilon}_{\lambda INT}(t)$, respectively. Boslough (1985) also implicitly assumes $r_{\lambda INT} = 0$ in (2). Although the absorption coefficients and reflectivities are written without an explicit dependence on λ, they may be wavelength-dependent, as discussed below.

Of all parameters influencing $I_{\lambda mod}(\lambda, t)$, only $T_{INT}(t)$ is assumed to be potentially time-dependent. This clearly complicates the time-dependence of the observed radiation. In addition, through the Planck function, $T_{INT}(t)$ can influence the wavelength-dependence of $I_{\lambda mod}(\lambda, t)$ with time. A number of models for $T_{INT}(t)$ are considered by Grover & Urtiew (1974) and Svendsen (1987). For completeness, and a basis for assumption, we outline one of these models, presumed appropriate to the MgO experiments discussed in this work. Assume that (i) energy transport is predominantly-parallel to the direction of shock propagation (i.e. one-dimensional), (ii) conduction is the only energy transport process that substantially affects the temperature in any part of the target on the time scale of the experiment, and (iii) shock compression/release processes in the target establish an initial ($t = 0$) temperature profile in the Ta–Ag–MgO system of the form

$$T(x, 0) \equiv \begin{cases} T_{Ta} & -\infty < x < -\delta \\ T_{Ag} & -\delta < x < 0 \\ T_{MgO} & 0 < x < \infty, \end{cases} \tag{8}$$

where δ is the film thickness. Note that we assume the driver plate (Ta) and MgO are thermal half-spaces. This last assumption presumes that shock compression/release is much faster than conduction in any part of the target. T_{Ta} and T_{Ag} are the temperatures of the partially-released Ta and Ag, both at the pressure of the Ag–MgO interface (i.e. pressure of the shock-compressed MgO). In the context of this model, all material properties of each target component are constants, and referenced to their respective states at the pressure of the Ag–MgO interface.

The temperature of a singly shock-compressed material, T_H, may be estimated from a classical thermodynamic energy balance (e.g. Ahrens, Anderson & Ringwood 1969; Jeanloz & Ahrens 1980b; see Svendsen 1987 for details), in which we assume the material compresses as an elastic fluid. It is possible that Ta (above ~295 GPa: Brown & Shaner 1984) and Ag ($\lesssim$ 185 GPa: Lyzenga 1980) melt in the range of pressures and temperatures achieved in our experiments. The data of Carter *et al.* (1971), Vassiliou & Ahrens (1981; and our results below) show no clearly-resolvable phase transition in MgO below 200 GPa. For simplicity, we assume that Ta and Ag do not change phase in our experiments. If this is wrong, the values of T_H we estimate for Ta and Ag are upper bounds to the true shock-compressed temperature (everything else being equal), since shock-induced phase transformations use energy otherwise available for heating the material. In the absence of phase changes, then, our estimate of T_H is given by

$$T_H = \left(T_s - \frac{1}{c_v}\Delta e_s\right) + \frac{1}{2c_v}\left\{\frac{1}{\rho_i} - \frac{1}{\rho_H}\right\} P_H, \tag{9}$$

assuming that c_v, the specific heat at constant volume of the shock-compressed state, is independent of temperature. The subscripts, *i*, *H*, *S* and *V* designate initial (STP), shock-compressed, constant entropy and constant volume states of the material, respectively. In (9), Δe_s is the change in specific internal energy of the material compressed isentropically (at specific entropy s_i) from its density at STP, ρ_i, to a density ρ_H (that of the shock-compressed state), while T_s is the temperature of the material along the isentrope referenced to s_i and ρ_i. Also, P_H is the pressure of the shock-compressed state.

We calculate ρ_H from the balance of mass and momentum across (i) the shock front in each target material, and (ii) the material boundaries between the target materials (impedance match: Rice, McQueen & Walsh 1958), by making the constitutive assumption that the component of the shock-wave velocity normal to the shock-front, U is a function of the change in the normal component of the material velocity, v, across the shock front. On the basis of the U–v data for Ta, Ag and MgO, we assume that U is a linear function of v (Table 1). The change in temperature along the compression isentrope, T_s, may be estimated from the classical thermodynamic Grüneisen's parameter, γ, via the relation

$$\gamma \equiv \left\{\frac{\partial \ln T}{\partial \ln \rho}\right\}_s . \qquad (10)$$

Since we assume $\gamma\rho$ is constant in all model calculations, this relation integrates to

$$T_s = T(s_i, \rho_H) \equiv T(s_i, \rho_i) \exp\left\{\gamma(\rho_i)\left(1 - \frac{\rho_i}{\rho_H}\right)\right\} .$$

Relations (9) and (10) imply that T_H is dependent on γ only indirectly, through T_s. We estimate Δe_s from a third-order spatial finite-strain parameterization (e.g. Davies 1973). Consequently, $\Delta e_s = \Delta e_s(\rho_i/\rho_H, K_{s_i}, K'_{s_i})$, where K_{s_i} and K'_{s_i} are the (STP) isentropic bulk modulus and its first pressure derivative, respectively, of the material (Table 1).

Table 1. Standard temperature and pressure (STP) parameters.

Property	Symbol	Ta	Ag	MgO	Units
Density	ρ	16.676[a]	10.501[a]	3.583[a]	Mg m^{-3}
Intercept of U–v relation‡	a	3.293[b] (±0.049)†	3.27[c]	6.61[d] (±0.06)	km s^{-1}
Slope of U–v relation	b	1.307[b] (±0.025)	1.55[c]	1.36[d] (±0.02)	
Bulk modulus	K_S	180.8[e]	109.6[e]	162.7[f] (±0.2)	GPa
$(\partial K_S/\partial P)_S$	K'_S	4.23[g]	5.20[g]	4.27[d] (±0.24)	
Specific heat at constant pressure	c_P	140.2[a]	235.5[a]	937.4[a]	J kg^{-1} K
Coefficient of thermal expansion	α	1.8[h]	5.7[h]	2.7[h]	$\times 10^{-5}$ K^{-1}
Melting temperature	T_M	3287[a]	1234[a]	3125[a]	K
Thermodynamic Grüneisen's parameter	γ	1.4[i]	2.5[i]	1.3[i]	
Thermal conductivity	k	57.5[j]	427[j]	60[j]	W m^{-1} K
Elastic Debye temperature	θ_D	263.8[k]	226.4[k]	942[l]	K

† Uncertainties as quoted in source, ‡ i.e. $U = a + bv$, *a* Robie, Hemingway & Fisher (1978), *b* Mitchell & Nellis (1981), *c* LASL compendium (1980), *d* Vassiliou & Ahrens (1981), *e* Calculated assuming $K_S \equiv \rho a^2$, *f* Jackson & Niesler (1981), *g* Calculated assuming $K'_S \equiv 4b - 1$, *h* Touloukian *et al.* (1975), *i* Calculated from $\gamma \equiv \alpha K_S/\rho c_P$, *j* Touloukian *et al.* (1970a), *k* Alers (1965), *l* Kieffer (1979).

As stated above, T_{Ta} and T_{Ag} are the temperatures of Ta and Ag at the pressure of shock-compressed MgO. We estimate the change in temperature due to release of Ta and Ag from their respective shock-compressed states, to their respective released states, by assuming that release occurs isentropically. This allows us to use (10), assuming no phase transitions occur during release. Also, we assume that each interface is smooth (Urtiew & Grover 1974; Svendsen, Bass & Ahrens 1987) in the sense that the shock-front is thicker than the interface 'gap' (Urtiew & Grover 1974) due to roughness of the surfaces forming the interface. This is consistent with the expectation that the Ag–MgO interface should be smooth, as discussed above. At this idealized interface, Ta releases directly to the pressure of shock-compressed Ag, and then both Ta and Ag release to the pressure of shock-compressed MgO.

To calculate the release temperature, we need the density of Ag and Ta in their respective release states. We estimate this using the variational method of Lyzenga & Ahrens (1978) to obtain a lower bound on the density of the chosen release state. This gives us, in turn, a lower bound on the temperature of that state through (10). As with the calculations of T_H, we neglect the effects of phase transitions driven by release and/or recompression on the resulting interface temperature.

As boundary conditions, we assume that the temperature and energy flux are continuous across the Ta–Ag and Ag–MgO interfaces, and use (8) to solve for the Ag–MgO interface temperature, $T_{INT}(t)$, i.e.

$$T_{INT}(t) = T_{Ag} + \frac{2\sigma_{Ta|Ag}(T_{Ta} - T_{Ag})}{(1 + \sigma_{MgO|Ag})(1 + \sigma_{Ta|Ag})}\phi(t) - \frac{\sigma_{MgO|Ag}(T_{Ag} - T_{MgO})}{(1 + \sigma_{MgO|Ag})}\psi(t). \quad (11)$$

In (11), we have

$$\phi(t) \equiv \sum_{m=0}^{\infty} (\nu_{MgO|Ag}\nu_{Ta|Ag})^m \operatorname{erfc}\left[(m + \tfrac{1}{2})\xi\sqrt{t_{exp}/t}\right]$$

and

$$\psi(t) \equiv 1 - \nu_{Ta|Ag} \operatorname{erfc}\left[\xi\sqrt{t_{exp}/t}\right] + \sum_{m=1}^{\infty} (\nu_{MgO|Ag}\nu_{Ta|Ag})^m \theta_m(t)$$

with

$$\theta_m(t) \equiv \operatorname{erfc}\left[m\xi\sqrt{t_{exp}/t}\right] - \nu_{Ta|Ag} \operatorname{erfc}\left[(m + 1)\xi\sqrt{t_{exp}/t}\right].$$

Also in (11), $\xi \equiv \delta/\sqrt{k_{Ag}\, t_{exp}}$, while

$$\sigma_{Ta|Ag} \equiv \left\{\frac{k_{Ta}\rho_{Ta}c_{P,Ta}}{k_{Ag}\rho_{Ag}c_{P,Ag}}\right\}^{1/2} \quad (12)$$

and

$$\sigma_{MgO|Ag} \equiv \left\{\frac{k_{MgO}\rho_{MgO}c_{P,MgO}}{k_{Ag}\rho_{Ag}c_{P,Ag}}\right\}^{1/2} \quad (13)$$

are the thermal-inertia 'mismatches' (Carslaw & Jaeger 1959, p. 321) between Ta and Ag, and between MgO and Ag, respectively, at the pressure of the Ag–MgO interface. The parameters $\nu_{MgO|Ag}$ and $\nu_{Ta|Ag}$ represent combinations of $\sigma_{MgO|Ag}$ and $\sigma_{Ta|Ag}$, respectively, i.e.

$$\nu_{MgO|Ag} \equiv \frac{(\sigma_{MgO|Ag} - 1)}{(\sigma_{MgO|Ag} + 1)}$$

and

$$\nu_{\mathrm{Ta|Ag}} \equiv \frac{(\sigma_{\mathrm{Ta|Ag}} - 1)}{(\sigma_{\mathrm{Ta|Ag}} + 1)}.$$

In (12) and (13), k, ρ and c_P are the thermal conductivity, density and specific heat at constant pressure, respectively, of the designated material and appropriate state of each material at the pressure of shock-compressed MgO. To estimate the values of $\sigma_{\mathrm{Ta|Ag}}$ and $\sigma_{\mathrm{MgO|Ag}}$ at high pressure, we need the appropriate values of k, ρ and c_P. The densities result from the impedance match and/or isentropic release calculations, while the high-pressure specific heats at constant pressure come from the relation

$$c_P = 3nR(1 + \alpha\gamma T)/M, \tag{14}$$

where n is the number of atoms in the formular unit, M is the molecular weight, R is the gas constant, and α is the thermal expansion (assumed independent of pressure and temperature). Note that we assume the high-temperature limit for c_v which is $(3nR/M)$. In the context of the Debye model, this presumes that all target components are well-above their Debye temperatures (STP values are given in Table 1). In addition, this assumes that the electronic contributions to c_v are small relative to $3nR/M$. Since the lowest-order electronic contribution to c_v scales with temperature, c_v would be larger than assumed here if these contributions are significant. If this is true, our estimates of both c_v and c_P will be too low, while the temperatures will be too high, at a given pressure.

Assuming that k_{Ta} and k_{Ag} are dominated by their electronic contributions, we assume the relevance of the Wiedemann–Franz–Lorenz (WFL) relation

$$\frac{\rho_e k}{T} = 2.45 \times 10^{-8}\ \mathrm{W} \cdot \Omega/\mathrm{K}^2 \tag{15}$$

(e.g. Berman 1976), where ρ_e is the electrical resistivity, to estimate k_{Ta} and k_{Ag} from electrical resistance data for shocked-Ta and Ag, respectively. Shock data exist for Ag (Dick & Styris 1975) up to 12 GPa, but not for Ta. Bridgman (1952) investigated the change in electrical resistance of many statically-compressed materials, including Ta and Ag, but again only at low pressure ($\lesssim 10$ GPa). Keeler (1971) investigated the change in the electrical resistance of shock-compressed copper and iron up to 140 GPa. He found that the resistivity of shock-compressed Cu decreased from ≈ 1.67 to $0.56\,\mu\Omega \cdot$ cm with pressure up to ≈ 100 GPa; a datum at 140 GPa implies that the resistivity of Cu reaches a minimum between 100 and 140 GPa and then increases to $\approx 0.83\,\mu\Omega \cdot$ cm at 140 GPa. As for Fe, the data imply that its electrical resistivity decreases from ≈ 2.5 to $0.47\,\mu\Omega \cdot$ cm between 13 and 140 GPa (above the $\alpha \rightarrow \epsilon$ transition). In light of (15), these trends imply that the thermal conductivities of shock-compressed Cu and Fe increase with shock pressure. On the basis of the behaviour of Cu, we assume that the electrical conductivity of Ta and Ag generally increases with shock pressure. Then, from (15), we see that a calculation of k_{Ta} and k_{Ag} using the STP electrical resistivities ($\rho_{e,\mathrm{Ta}} = 12.45\,\mu\Omega \cdot$ cm and $\rho_{e,\mathrm{Ag}} = 1.59\,\mu\Omega \cdot$ cm: Weast 1979), along with the appropriate release-state temperatures of Ta and Ag, respectively, will give us a lower bound on these thermal conductivities. As for k_{MgO}, we assume it is dominated by its lattice component at high pressure, and use the lattice thermal-conductivity model of Roufosse & Klemens (1974) to estimate it. This assumption is supported by band-gap calculations for MgO (e.g. Liberman 1978), and, in view of (15), by the results of Ahrens (1966), which suggest that the electrical resistivity of MgO is $\sim 10^9\,\mu\Omega \cdot$ cm above 92 ± 7 GPa.

Having established the means, we calculate selected model parameters at high pressure

Table 2. Model parameter estimates for MgO experiments.

		Shock-compressed state			Ag–MgO interface state			
Shot	Material	P (GPa)	T (K)	ρ (Mg m^{-3})	T (K)	ρ (Mg m^{-3})	k W m^{-1} K)	c_P (J kg^{-1} K)
166	Ta	336.6	14430	28.130	11860	22.750	2336.0	165
	Ag	277.7	13560	17.190	11400	15.440	17600.0	487
	MgO	174.0	2913	5.345	2913	5.345	32.6	1324
147	Ta	349.1	15320	28.350	12600	22.90	2477.0	167
	Ag	288.2	14330	17.290	12060	15.53	18570.0	500
	MgO	181.1	3032	5.426	3028	5.43	32.1	1326
145	Ta	364.3	16420	28.600	13470	23.010	2651.0	169
	Ag	300.9	15270	17.410	12810	15.590	19760.0	516
	MgO	187.9	3257	5.442	3257	5.442	31.5	1332
146	Ta	395.0	18730	29.130	15320	23.280	3014.0	173
	Ag	326.7	17240	17.640	14420	15.750	22230.0	548
	MgO	203.1	3667	5.536	3667	5.536	30.5	1342

from the STP parameters given in Table 1 and list the results for each experiment in Table 2. From the impedance match and partial-release calculations, we obtain the density of Ta, Ag and MgO at the pressure shock-compressed MgO, and from these, through (8) and (9), we obtain T_{Ta}, T_{Ag} and T_{MgO} for each experiment. Using these with (14), (15) and the model of Roufosse & Klemens (1974), we estimate $\sigma_{MgO|Ag}$ and $\sigma_{Ta|Ag}$ for each experiment and compare them with their STP values in Table 3. Also, we have calculated $\sigma_{MgO|Ag}$ and $\sigma_{Ta|Ag}$ as a function of Ag–MgO interface conditions (pressure) and displayed them in Fig. 4. Again, the values of k for each materials, especially the metals, are probably the most uncertain aspect of these estimates. On this basis, we see that $\sigma_{Ta|Ag}$ is approximately independent of pressure and temperature. However, $\sigma_{MgO|Ag}$ decreases steadily from approximately 0.44 at STP to 0.03 at 200 GPa, mainly because of the large increase in k_{Ag} (Tables 1 and 2).

From (11), the initial value of $T_{INT}(t)$ is given by

$$T_{INT}(0) = T_{Ag} - \frac{\sigma_{MgO|Ag}(T_{Ag} - T_{MgO})}{(1 + \sigma_{MgO|Ag})}. \tag{16}$$

This is also the value of $T_{INT}(t)$ with $\xi = \infty$. For $t = \infty$ or $\xi = 0$, $T_{INT}(t)$ is given by

$$T_{INT}(\infty) = T_{Ag} + \frac{2[\sigma_{Ta|Ag}(T_{Ta} - T_{Ag}) - \sigma_{MgO|Ag}(T_{Ag} - T_{MgO})]}{(1 + \sigma_{Ta|Ag})(1 + \sigma_{MgO|Ag})} \sum_{m=0}^{\infty} (\nu_{Ta|Ag}\nu_{MgO|Ag})^m. \tag{17}$$

Table 3. Thermal mismatch estimates for MgO experiments and at STP.

Conditions	$\sigma_{Ta\|Ag}$	$\sigma_{MgO\|Ag}$
STP	0.36	0.44
Shot 166	0.26	0.04
Shot 147	0.26	0.04
Shot 145	0.25	0.04
Shot 146	0.25	0.03

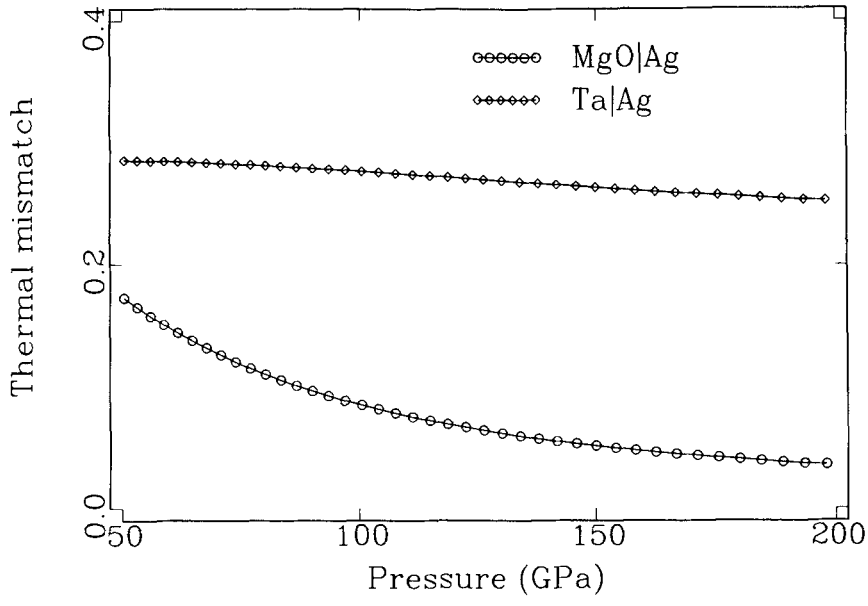

Figure 4. Estimates of $\sigma_{Ta|Ag}$ and $\sigma_{MgO|Ag}$ as a function of the Ag–MgO interface pressure. The decrease of $\sigma_{MgO|Ag}$ with pressure is due to the temperature-dependence of the Wiedemann–Franz–Lorenz thermal-conductivity parameterization for Ta and Ag given in the text, causing k_{Ta} and k_{Ag} to increase with pressure. These curves are lower bounds to $\sigma_{Ta|Ag}$ and $\sigma_{MgO|Ag}$ if k_{Ta} and k_{Ag} become independent of temperature at high pressure (see text).

For shot 146 conditions, $T_{INT}(0) = 14070$ K and $T_{INT}(\infty) = 13910$ K. Note that $T_{INT}(t)$ is bounded below by $T_{INT}(\infty)$ in this case. The time-dependence of $T_{INT}(t)$, embodied in $\phi(t)$ and $\psi(t)$, can more easily be seen in the following approximations to $T_{INT}(t)$. For $\xi \to 0$, $\phi(t)$ and $\theta_m(t)$ are given by

$$\phi(t) \sim \sum_{m=0}^{\infty} (\nu_{Ta|Ag}\nu_{MgO|Ag})^m \left\{1 - (2m+1)\xi\left(\frac{t_{exp}}{\pi t}\right)^{1/2} \exp\left[-(m+\tfrac{1}{2})^2\xi^2 t_{exp}/t\right]\right\} \tag{18}$$

and

$$\psi(t) \sim (1 - \nu_{Ta|Ag}) + 2\nu_{Ta|Ag}\xi\left(\frac{t_{exp}}{\pi t}\right)^{1/2} + \sum_{m=1}^{\infty} (\nu_{MgO|Ag}\nu_{Ta|Ag})^m \theta_m(t),$$

with

$$\theta_m(t) \sim (1 - \nu_{Ta|Ag}) - 2\nu_{Ta|Ag}\xi\left(\frac{t_{exp}}{\pi t}\right)^{1/2} \left\{m \exp\left(-m^2\xi^2 t_{exp}/t\right)\right.$$

$$\left. - \nu_{Ta|Ag}(m+1) \exp\left[-(m+1)^2\xi^2 t_{exp}/t\right]\right\} .$$

In addition, for $\xi \to \infty$, we have

$$\phi(t) \sim \frac{1}{\xi}\left(\frac{t}{\pi t_{exp}}\right)^{1/2} \sum_{m=0}^{\infty} (\nu_{Ta|Ag}\nu_{MgO|Ag})^m \frac{1}{(m+\tfrac{1}{2})} \exp\left[-(m+\tfrac{1}{2})^2\xi^2 t_{exp}/t\right] \tag{19}$$

and

$$\psi(t) \sim 1 - \frac{\nu_{\mathrm{Ta|Ag}}}{\xi}\left(\frac{t}{\pi t_{\mathrm{exp}}}\right)^{1/2} \exp\left(-\xi^2 t_{\mathrm{exp}}/t\right) + \sum_{m=1}^{\infty} \left(\nu_{\mathrm{MgO|Ag}}\nu_{\mathrm{Ta|Ag}}\right)^m \theta_m(t)$$

with

$$\theta_m(t) \sim \frac{1}{\xi}\left(\frac{t}{\pi t_{\mathrm{exp}}}\right)^{1/2}\left\{\frac{1}{m}\exp\left(-m^2\xi^2 t_{\mathrm{exp}}/t\right) - \frac{\nu_{\mathrm{Ta|Ag}}}{(m+1)}\exp\left[-(m+1)^2\xi^2 t_{\mathrm{exp}}/t\right]\right\}.$$

From the parameters in Table 2, we have $\sqrt{k_{\mathrm{Ag}}t_{\mathrm{exp}}} \sim 10^{-5}$ m for shot 146 conditions; consequently, with $\delta \lesssim 10^{-6}$ m, we have a (conductively) thin film ($\xi \lesssim 0.1$). Using these estimates for shot 146 conditions, we display $T_{\mathrm{INT}}(t)$, calculated for 3 different values of ξ (1.0, 0.1 and 0.01), and $\sigma_{\mathrm{Ta|Ag}}$ and $\sigma_{\mathrm{MgO|Ag}}$ for the conditions of this shot (Table 3), in Fig. 5. We also plot the 2 approximations [$\xi \to 0$, (18), and $\xi \to \infty$, (19)] in this figure. Clearly, over the entire range of ξ, $T_{\mathrm{INT}}(t)$ lies within about 200 K of $T_{\mathrm{INT}}(0)$. In particular, with $\xi \lesssim 0.1$, $T_{\mathrm{INT}}(t)$ is essentially independent of time and approximately equal to $T_{\mathrm{INT}}(\infty)$. We note that $T_{\mathrm{INT}}(t)$ will approach T_{MgO} only if $\sigma_{\mathrm{MgO|Ag}} \gg 1$ ($k_{\mathrm{Ag}} \to 0$ or $k_{\mathrm{MgO}} \to \infty$) and $\xi \ll 1$. So, assuming our estimate of $\sigma_{\mathrm{MgO|Ag}}$ is reasonable, we have some justification for assuming that $T_{\mathrm{INT}}(t)$ is essentially constant, and approximately equal to $T_{\mathrm{INT}}(\infty)$, during the experiment.

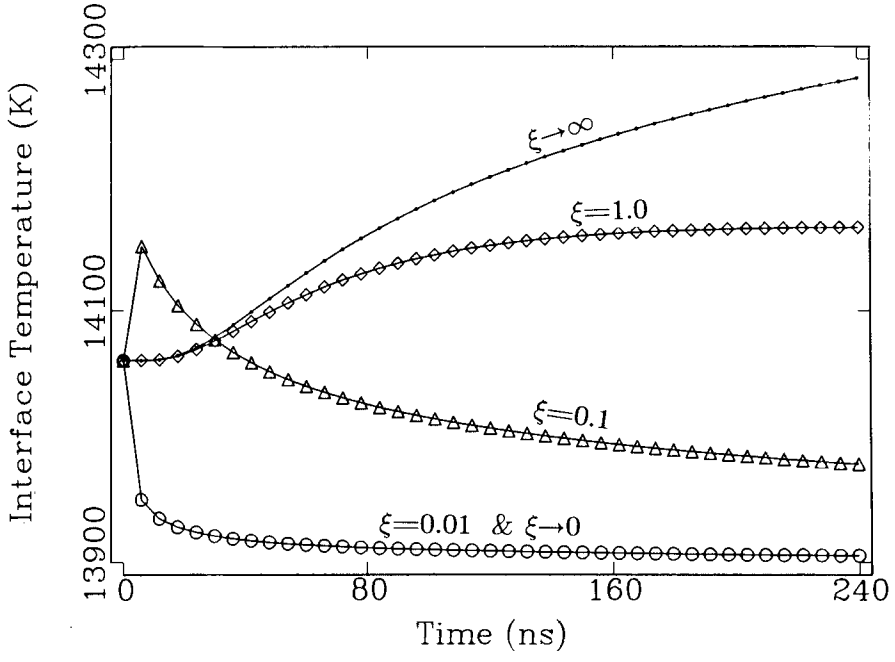

Figure 5. Model Ag–MgO interface temperature, $T_{\mathrm{INT}}(t)$, as a function of time for different non-dimensional Ag-film thicknesses, $\xi = \delta/\sqrt{k_{\mathrm{Ag}}t_{\mathrm{exp}}}$, where δ is the Ag-film thickness and k_{Ag} its thermal conductivity at the Ag–MgO interface pressure. This calculation is for shot 146 conditions, with $\sigma_{\mathrm{Ta|Ag}} = 0.25$, $\sigma_{\mathrm{MgO|Ag}} = 0.03$, $T_{\mathrm{Ta}} = 15320$ K, $T_{\mathrm{Ag}} = 14420$ K, and $T_{\mathrm{MgO}} = 3667$ K (Table 2). From these, we have $T_{\mathrm{INT}}(t = 0) = 14070$ K and $T_{\mathrm{INT}}(t = \infty) = 13910$ K, as defined in the text. The circles represent $\xi = 0.01$ and $\xi \to 0$ [the latter from (18) in text, respectively, while the diamonds and dots are for $\xi = 1.0$ and $\xi \to \infty$ (19) in text], respectively.

Table 4. Radiation model parameters† for shot 146.

Wavelength (nm)	$a_{\lambda MgO,O}$‡ (m^{-1})	$r_{\lambda SF}$	$a_{\lambda MgO}$ (m^{-1})	$r_{\lambda INT}$
450	68.0	0.1	6300	0.9
600	82.0	0.3	7500	0.2
750	97.0	0.1	4200	0.6
900	128.0	0.1	3800	0.5

† – T_{INT} = 20 000 K, T_{MgO} = 3667 K, and $r_{\lambda FS}$ = 0.08 at all wavelengths in fit. $r_{\lambda FS}$ was calculated from $n_{\lambda MgO}$ = 1.736 (Weast 1979) and formula for effective normal spectral reflectivity given in text; ‡ – calculated from data of Touloukian *et al.* (1970b) and d = 2.562 mm for shot 146 (Table 6).

With these consierations in mind, we display an example fit to the data for shot 146 in Fig. 6, assuming that $T_{INT}(t)$ is time-dependent. Assuming that our measurement errors are independently random, and normally-distributed around the model that actually fits the data, the 'best fit' to the data is achieved through minimization of the function $\chi^2(\lambda)$, given by

$$\chi^2(\lambda) = \chi^2[\lambda; r_{\lambda SF}, a_{\lambda MgO}, r_{\lambda INT}, T_{INT}] \equiv \frac{1}{[\sigma(\lambda)]^2} \sum_t [I_{\lambda exp}(\lambda, t) - I_{\lambda mod}(\lambda, t)]^2, \quad (20)$$

(e.g. Press *et al.* 1986), where $\sigma(\lambda)$ is the uncertainty of the data at wavelength λ. Using a golden section (GS) search technique (e.g. Press *et al.* (1986)), we fit $I_{\lambda mod}(\lambda, t)$ to $I_{\lambda exp}(\lambda, t)$ by fixing $r_{\lambda FS}$, $a_{\lambda MgO,O}$ to known values (Table 4), and T_{MgO} to its value as given by (9) and the parameters in Table 1. Fixing T_{MgO} to this value is justified by agreement with the results of greybody fits discussed below. In addition, the fit results are not sensitive to T_{MgO} in this case (Svendsen 1987). In this case, we vary $r_{\lambda SF}$, $a_{\lambda MgO}$, $r_{\lambda INT}$ and T_{INT} to minimize $\chi^2(\lambda)$. Even though the fit using (20) will produce λ-dependent optical parameters as the data allows, we really cannot quantitatively assess (i) the ability of the data to resolve the wavelength-dependence of these parameters, (ii) whether we have too many or few free parameters (even though they are all physically well-established), and (iii) whether we have over- or under-estimated measurement uncertainties, all because the data lacks sufficient wavelength-resolution (i.e. we have four wavelength-dependent parameters and data at four wavelengths). In fact, all we can really resolve is the wavelength-averaged magnitude of the model parameters that are potentially wavelength-dependent. If we had sufficient wavelength-resolution, we could let all free parameters vary as allowed physically in (λ, t) space, and invert for their best values. However, the resolution of the data with respect to the wavelength-dependence of $r_{\lambda SF}$, $a_{\lambda MgO}$, $r_{\lambda INT}$ is, at best, poor. Keeping all this in mind, we display the results of this fit for shot 146 data in Table 4. Beyond the data resolution problem, we note that the potential wavelength-dependence of the parameters allowed to vary in the fit, (especially $a_{\lambda MgO}$) is also dependent on our assumption of constant $T_{INT}(t)$. From (2) and (3), we see that $T_{INT}(t)$, $a_{\lambda MgO,O}$ and $a_{\lambda MgO}$ control the slope and magnitude, while the effective reflectivities and T_{MgO} influence only the magnitude, of $I_{\lambda mod}(\lambda, t)$. With a fixed $a_{\lambda MgO,O}$, and $T_{INT} \gg T_{MgO}$, then, the fit is most sensitive to T_{INT} and $a_{\lambda MgO}$; these should be best resolved. The results of this fit (Table 4) suggest that shocked MgO at 200 GPa is $\sim$ 50–100 times more absorptive than at STP. Further, along with $r_{\lambda INT}$ (Table 4), $a_{\lambda MgO,O}$ may be wavelength-dependent. Also, we note that the fits favour a much larger T_{INT} ($\sim$20 000 K: Table 4)

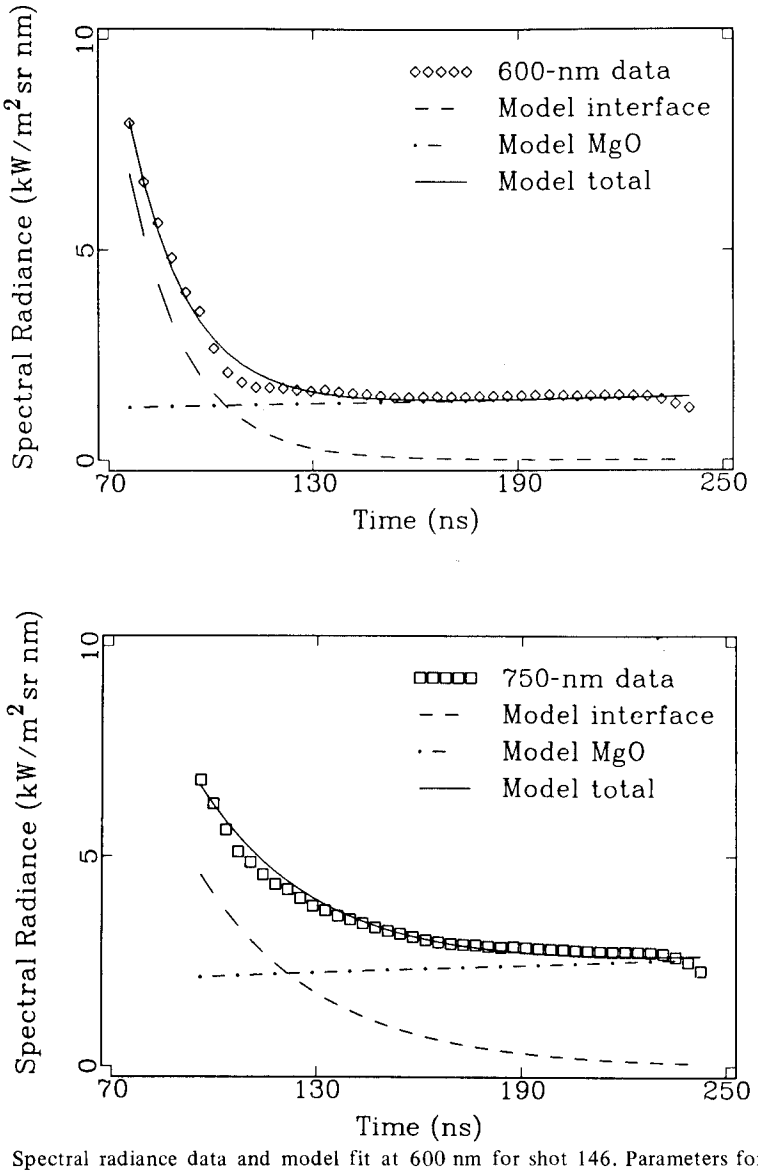

Figure 6. (a) Spectral radiance data and model fit at 600 nm for shot 146. Parameters for the fits are given in Table 4. The fit implies that the data are largely consistent with a high, time-independent interface temperature ($T_{INT} \sim 20\,000$ K for 146), strongly-absorbing shocked MgO (Table 4), and the estimated values for T_{MgO} (Table 2) used in the fits. It also implies that the contribution from the shocked MgO dominates that from Ag at the interface after $\approx$ 100 ns. (b) Spectral radiance data and model fit at 750 nm.

than $T_{INT}(0)$ calculated above for shot 146. This large value of T_{INT} implies that the Ag film is (i) is slightly porous (~8–10 per cent) and/or (ii) reshocked at the Ag–MgO interface (Urtiew & Grover 1974). Trapped gas at Ag–MgO interface as radiation source (Boslough 1985) seems unlikely since it was formed under vacuum. However, we cannot rule out the influence of processes (e.g. reshocking) at the Ta–Ag interface on T_{INT}. The decay of radiation intensity for shot 146 is progressively faster going toward shorter wavelengths

(i.e. from 900 to 450 nm: Fig. 3). This can happen if $T_{INT}(t)$ decays very strongly over time, and/or the effective spectral absorption-coefficient increases toward shorter wavelengths. We do not see a cross-over of the radiation intensities at shorter wavelengths, however, implying that a strong decay of $T_{INT}(t)$ to near T_{MgO} does not dominate the time-dependence of $T_{INT}(t)$. If $T_{INT}(t)$ does decay strongly, the magnitude of $a_{\lambda MgO}$ would be less and its wavelength-dependence different. In this sense, our assumption of constant T_{INT} has given us an upper bound on the magnitude of $a_{\lambda MgO}$.

In the context of our model, the effective normal spectral-reflectivity of the boundary between any two (dynamic) target components i and j is given by (e.g. Siegel & Howell 1980)

$$r_\lambda \equiv \frac{(n_{\lambda i} - n_{\lambda j})^2 + (\omega_{\lambda i} - \omega_{\lambda j})^2}{(n_{\lambda i} + n_{\lambda j})^2 + (\omega_{\lambda i} + \omega_{\lambda j})^2}.$$

In this relation, n_λ and ω_λ are the real and imaginary parts of the complex index of refraction of the material, and, as with all the other optical parameters, they are both potentially λ-dependent. ω_λ is also known as the electromagnetic extinction coefficient. The values of $r_{\lambda SF}$ from the fit imply that the refractive index of MgO changes very little upon shock compression up to 200 GPa. This is consistent with the low-pressure data of Vedam & Schmidt (1966), which implies that the refractive index of MgO actually decrease very slightly ($\sim 1.5 \times 10^{-3}\,\mathrm{GPa}^{-1}$) due to the decrease in electronic polarizability, which dominates the intrinsic increase in refractive index with pressure. The slightly-higher value of $r_{\lambda SF}$ at 600 nm is clearly warranted by the data (see below), and may represent a dependence of $n_{\lambda MgO}$ on wavelength. Noting that $a_{\lambda MgO} = 4\pi\omega_{\lambda MgO}/\lambda$ (e.g. Siegel & Howell 1981), where ω_{MgO} is the extinction coefficient of shocked MgO, our results imply that $\omega_{MgO} \sim 10^{-3}$, also consistent with a small value for $r_{\lambda SF}$. The values of $r_{\lambda INT}$ in Table 4 may be compared with $r_{\lambda INT}(600\,\mathrm{nm}) = 0.9$ at STP, calculated with $n_{\lambda Ag} = 0.18$, $\omega_{\lambda Ag} = 3.64$ at 600 nm (Svet 1965) and $n_{\lambda MgO} = 1.736$ (Table 4). Since $\omega_{\lambda MgO}$ appears to be too small to significantly affect $r_{\lambda INT}$, the decrease of $r_{\lambda INT}$ at high pressure implied by the fit may represent a change mainly in $n_{\lambda Ag}$ and/or $\omega_{\lambda Ag}$ with pressure.

The strongest result of this fit is that MgO is significantly more opaque at high pressure. This is consistent with the results of Gaffney & Ahrens (1973), who observed a wavelength-independence in opacity at 46.5 GPa in MgO. This change in opacity may be due to shock-induced defect structures, since MgO did not recover its transparency during release. With the possible exception of Al_2O_3 (Bass, Svendsen & Ahrens 1987; but see Urtiew 1974), all initially-transparent materials studied so far (e.g. Lif: Kormer 1968; $CaAl_2Si_2O_8$: Boslough *et al.* 1986) lose some transparency during shock compression. We note that a similar fit to shot 145 data is qualitatively consistent with that for shot 146 data.

To get more precise estimates of the optical parameters, we need further constraints on $\hat{\epsilon}_{\lambda INT}(t)$ and $T_{INT}(t)$. One possible means to this is the use of two recording systems during the experiment, one set to record the initial intensity of the interface radiation, and the other set to record the expected intensity of the sample radiation. In this way the early history of the radiation intensity should constrain the early time-dependence of $\hat{\epsilon}_{\lambda INT}(t)$ and $T_{INT}(t)$, before the optical properties of shocked MgO can significantly affect the observed radiation-intensity.

Having some understanding of the time- and wavelength-dependence of the observed radiation intensity, we can, with some justification, fit the greybody relation

$$I_{\lambda gb}(\lambda, t) \equiv \hat{\epsilon}_{fit}(t)\, I_{\lambda pl}[\lambda, T_{fit}(t)] \qquad (21)$$

at a given time, which we designate t_r, to the end of the observed radiation histories and find

the effective emissivity and temperature of shocked MgO. The choice of t_r is equal to the calculated shock-wave transit time through the MgO, but is not critically dependent on this choice, as we show below.

To fit $I_{\lambda gb}(\lambda, t)$ to the data, we again use the χ^2 measure. In this case, it is given by

$$\chi^2(t_r) = \chi^2[t_r; \hat{\epsilon}_{fit}, T_{fit}] \equiv \sum_{\lambda} \left\{ \frac{1}{[\sigma(\lambda)]^2} \left[I_{\lambda exp}(\lambda, t_r) - \hat{\epsilon}_{fit}(t_r) I_{\lambda pl}[\lambda, T_{fit}(t_r)] \right]^2 \right\} . \quad (22)$$

Unlike (20), the sum is now over all wavelengths observed in the experiment. On this basis, $\hat{\epsilon}_{exp}(t_r)$ and $T_{exp}(t_r)$ represent the values of $\hat{\epsilon}_{fit}(t_r)$ and $T_{fit}(t_r)$ that minimize $\chi^2(t_r)$. Since the fit is with respect to wavelength, the value of $\hat{\epsilon}_{exp}(t_r)$ represents a wavelength-average of $\hat{\epsilon}_{\lambda MgO}(\lambda, t_r)$. Since $\chi^2(t_r)$ is a nonlinear functional of temperature, we find its minimum numerically using (i) GS search, as above, and (ii) the method of Levenberg as formulated by Marquardt (LM). See, for example, Press *et al.* (1986), for details on both of these methods. To obtain starting values of $\hat{\epsilon}_{fit}(t)$ and $T_{fit}(t)$ for the nonlinear fit, we use Wien's approximation to $I_{\lambda pl}(\lambda, T)$ in $\chi^2(t_r)$, which follows from $I_{\lambda pl}(\lambda, T)$ in the limit $\exp(C_2/\lambda T) \gg 1$, i.e.

$$I_{\lambda wgb}(\lambda, t) \equiv \hat{\epsilon}_{fit}(t) I_{\lambda wi}(\lambda, t) = \hat{\epsilon}_{fit}(t) \frac{2C_1}{\lambda^5} \exp[-C_2/\lambda T_{fit}(t)] . \quad (22)$$

The relative error incurred in approximating $I_{\lambda pl}$ by $I_{\lambda wi}$ is equal to $\exp(-C_2/\lambda T)$; this approximation is accurate to within 1 per cent for $\lambda T < 3 \times 10^{-3}$ m·K (Siegel & Howell 1980). Since we can fit Wien's relation to the data via linear least-squares, we can solve for $\hat{\epsilon}_{fit}(t_r)$ and $T_{fit}(t_r)$ directly (i.e. without iteration).

We argue above that the radiation intensity at the end of the record likely represents only

Table 5. Greybody fits to radiation data at t_r.

		Uncorrected				Corrected			
Shot	Parameter (t_r)	Wien	GS	LM	GS ($\hat{\epsilon}_{fit}=1$)	Wien	GS	LM	GS ($\hat{\epsilon}_{fit}=1$)
166 (750,900)§	$\hat{\epsilon}_{exp}$(285 ns)	1.02 (0.22)	1.00 (0.022)†			1.23 (0.22)	1.18 (0.22)		
	T_{exp}(285 ns)		3046 (120)	3056 (120)		3054 (115)		3062 (120)	3081 (120)
	χ^2		0.001	0.0005		0.02		0.001	0.0005
147 (600)	T_{exp}(210 ns)				2981 (120)				3071 (130)
145 (all)	$\hat{\epsilon}_{exp}$(210 ns)	0.41 (0.80)	1.02 (0.80)	0.64 (0.18)‡		0.50 (0.80)	1.02 (0.80)	0.75 (0.21)	
	T_{exp}(210 ns)	3739	3174 (480)	3352 (355)	3186 (200)	3756 (355)	3281 (485)	3372 (375)	3292 (220)
	χ^2	9.68	7.29	8.70	7.33	9.69	7.58	8.77	7.62
146 (all)	$\hat{\epsilon}_{exp}$(200 ns)	0.88 (0.69)	1.04 (0.69)	1.17 (0.17)		1.07 (0.69)	1.21 (0.69)	1.42 (0.20)	
	T_{exp}(200 ns)	3735 (410)	3615 (385)	3530 (80)	3639 (390)	3757 (415)	3663 (395)	3549 (100)	3784 (420)
	χ^2	1.64	1.41	1.35	1.45	1.64	1.46	1.36	1.70

† – Golden section search fit. Uncertainties represent experimentally-based uncertainties. ‡ – Levenberg–Marquardt fit. Uncertainties represent standard deviations of corresponding fit. § – Wavelengths used in fit.

that of shocked MgO. In this case, from relations (1) and (2), we also see that, with $\hat{\epsilon}_{\lambda INT}(\lambda, t = t_r \approx t_{exp}) \approx 0 \ll \hat{\epsilon}_{\lambda MgO}(\lambda, t_r)$,

$$I_{\lambda mod}(\lambda, t_r) \approx \hat{\epsilon}_{\lambda MgO}(t_r)\, I_{\lambda pl}(\lambda, T_{MgO}) \tag{23}$$

with

$$\hat{\epsilon}_{\lambda MgO}(t_r) \approx (1 - r_{\lambda FS})(1 - r_{\lambda SF})\,[1 + r_{\lambda INT} \exp(-a^*_{\lambda MgO})]\,[1 - \exp(-a^*_{\lambda MgO})]. \tag{24}$$

Recalling that $r_{\lambda FS}$ is independently established (Table 4), and making the values of $r_{\lambda SF}$, $a^*_{\lambda MgO}$ and $r_{\lambda INT}$ established by the model fit, we may 'correct' the radiation data and fit

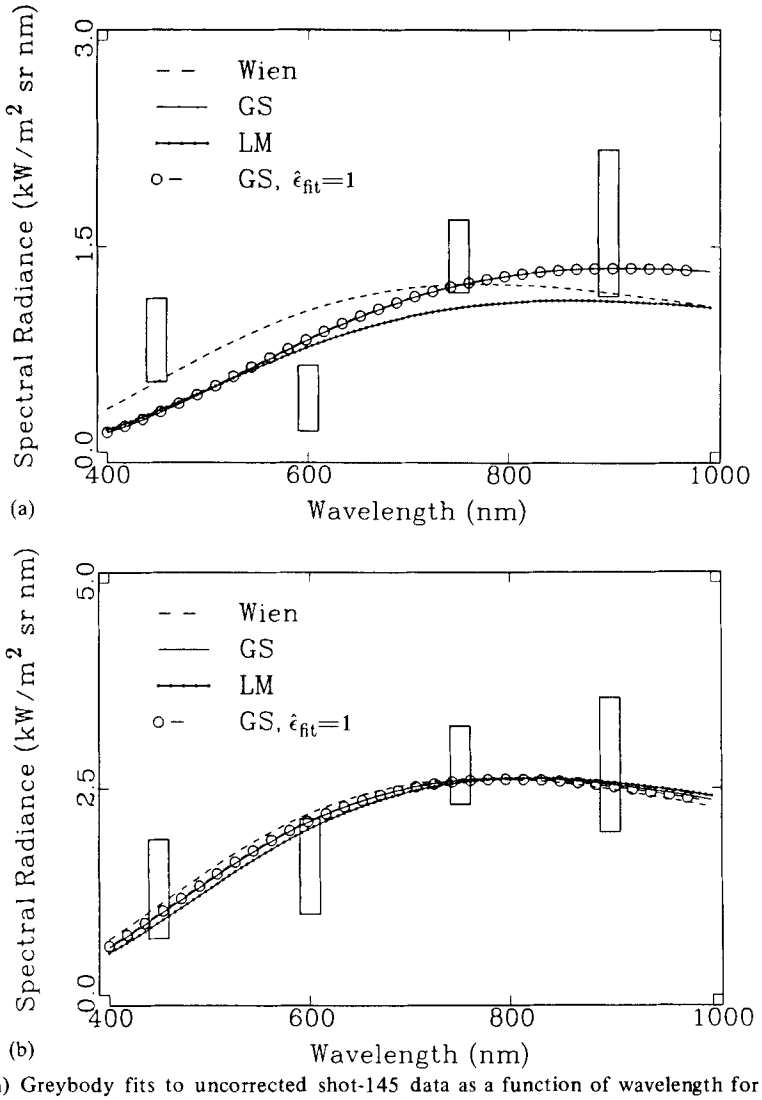

Figure 7. (a) Greybody fits to uncorrected shot-145 data as a function of wavelength for $\hat{\epsilon}_{exp}(t_r)$ and $T_{exp}(t_r)$. The size of the data rectangles represent experimental uncertainty. Note the deviation (i.e. outside experimental uncertainty) at 600 nm of the spectral radiance below the various fits. (b) Greybody fits to uncorrected shot-146 data. As with shot 145, the datum at 600 nm falls below the fits. This observation is substantiated as a larger value of $r_{\lambda FS}$(600 nm) (Table 4) in the fit of Fig. 6(b) at 600 nm.

for $\hat{\epsilon}_{exp}(t_r)$ $T_{exp}(t_r)$ as above. This is a somewhat-crude way of correcting for apparent λ-dependence of $\hat{\epsilon}_{\lambda MgO}$ from the fit using (20) discussed above. In principle, this should allow us to fit for $T_{exp}(t_r)$ alone, but we allow $\hat{\epsilon}_{exp}(t_r)$ to vary because we set $\hat{\epsilon}_{exp}(t_r) = 1$ in one of the GS fits already (i.e. out of curiosity).

Unlike the previous fit, we have four data and two parameters (at least for shots 145 and 146) in the greybody fit. However, we are still confined to wavelength-average values for $\hat{\epsilon}_{exp}(t_r)$. We present the results of both the corrected – using (23)–(24) – and uncorrected fits in Table 5, and plot the uncorrected fit for shots 145 and 146 in Fig. 7(a) and (b), respectively. The results for shot 166 (Table 5) do not include a LM fit because the method requires at least 3 data points for a fit to two parameters. The uncertainties associated with the GS fits represent measurement uncertainties mapped into uncertainties for $\hat{\epsilon}_{exp}(t_r)$ and $T_{exp}(t_r)$ through use of (25)–(28) given below. However, the uncertainty associated with each LM fit is the standard deviation of that fit. Roughly speaking, the values of $\chi^2(t_r)$ given in Table 5 can be compared to the number of data minus the number of parameters in the fit to judge its 'goodness'. On this basis, the fit for shot 145 is not as 'good' as that for 166, and especially 146. The experimental uncertainties for shots 166 and 147 are much lower, of course, mainly because they are based on only two wavelengths and a single wavelength, respectively. For shots 145 and 146, within the fit uncertainty, the LM and GS results agree (Table 5). Also, there is, within uncertainty, no difference between the corrected and uncorrected results (the corrected-data results are slightly closer to the calculated values of T_{MgO} as listed in Table 2). Except for the shot-145 LM results, the effective emissivities of the LM and GS fits are ≥ 1, and unphysical result. However, the associated data and fit uncertainties easily allow the effective emissivities to be less than unity. Also, as noted by Boslough *et al.* (1986), $\hat{\epsilon}_{fit}$ is much more sensitive to data scatter (in λ and/or t), whether due to uncorrected wavelength-dependences in the data, or experimental measurement errors. This results from the functional form of $I_{\lambda gb}$, as can be seen from the following relations:

$$\frac{\delta T_{fit}}{T_{fit}} \approx \left(\frac{\partial \ln T_{fit}}{\partial \ln I_{\lambda gb}}\right)_{\hat{\epsilon}_{fit},\lambda} \frac{\delta I_{\lambda gb}}{I_{\lambda gb}} \tag{25}$$

and

$$\frac{\delta \hat{\epsilon}_{fit}}{\hat{\epsilon}_{fit}} \approx \left(\frac{\partial \ln \hat{\epsilon}_{fit}}{\partial \ln I_{\lambda gb}}\right)_{T_{fit},\lambda} \frac{\delta I_{\lambda gb}}{I_{\lambda gb}}, \tag{26}$$

where

$$\left(\frac{\partial \ln T_{fit}}{\partial \ln I_{\lambda gb}}\right)_{\hat{\epsilon}_{fit},\lambda} = \frac{\mu}{(1+\mu)\ln(1+\mu)} < 1, \quad \mu > 0 \tag{27}$$

$$\left(\frac{\partial \ln \hat{\epsilon}_{fit}}{\partial \ln I_{\lambda gb}}\right)_{T_{fit},\lambda} = 1 \tag{28}$$

and

$$\mu = \frac{2C_1 \hat{\epsilon}_{fit}}{\lambda^5 I_{\lambda gb}}$$

(note that λ and $\hat{\epsilon}_{fit}$ are fixed in this last relation). From these relations we see that a given variation of $I_{\lambda exp}$, and hence $I_{\lambda gb}$ in the fit, will have a larger impact on $\hat{\epsilon}_{fit}$ than T, i.e. $\delta T_{fit}/T_{fit} < \delta\hat{\epsilon}_{fit}/\hat{\epsilon}_{fit}$ for all $\delta I_{\lambda gb}/I_{\lambda gb}$. Consequently, it is not surprising that $\hat{\epsilon}_{exp}(t_r)$ cold be greater than unity with any significant scatter, if not constrained to be less than or equal to unity in the fit.

The fits displayed in Fig. 7(a) and (b) for shots 145 and 146, respectively, both show that the 600-nm data lie significantly below the fits. This is also suggested by the model results displayed in Fig. 6 for shot 146, where $r_{\lambda SF}(600\text{ nm}) = 0.3$. This deviation probably does not represent systematic error, since we have never seen anything like it in the data from other experiments of this nature. That it reflects a property of shock-compressed MgO is supported by the radiation spectrum of shock-compressed MgO at 60 GPa (Schmitt & Ahrens 1984), which is non-thermal and displays a sharp drop in intensity below ~650 nm, possibly due to λ-dependent absorption and/or reflectivity. This possibility is consistent with the results of the fit displayed in Table 4. This apparent non-blackbody trend in the MgO data is one possible cause of 'data scatter' leading to non-physical values of $\hat{\epsilon}_{fit}$, as discussed above.

That our choice of t_r, within a given window of time, is not essential to our results can be shown by fitting a window of time around t_r and displaying the consequences. We do this for shot 146 uncorrected data and display the results in Fig. 8. As evident, the fit is essentially time-independent 10 ns on either side of t_r. This is true for the fits to shots 166 and 145 as well.

Discussion

In Table 6, we list the greybody fit and uncertainties, along with the calculated shock-wave velocities, shock-transit times, pressure and temperature, for each experiment. The uncertainties of calculated quantities are based on a propagation of the parameter uncertainties listed in Table 1 through the calculation of each quantity. The values of $\hat{\epsilon}_{exp}(t_r)$ and $T_{exp}(t_r)$ in Table 6 are those for the GS fit with $\hat{\epsilon}_{fit}$ and T_{fit} variable, which

Table 6. Experimental results and model estimates.

Shot	Experimental results					Model estimates				
	ρ (Mg m^{-3})	d (mm)	v_{imp} (km s^{-1})	$\hat{\epsilon}_{exp}$	T_{exp} (K)	t_r (ns)	U (km s^{-1})	t_{st} (ns)	P_{MgO} (GPa)	T_{MgO} (K)
166	3.562	3.468	5.73	1.18	3081	285	12.10	286.6	174.0	2913
	(0.002)†	(0.005)	(0.04)	(0.22)	(120)	(10)	(0.14)	(3.4)	(2.6)	(415)
147	3.595	2.513	5.87	1.00	3071	205	12.22	205.7	181.1	3028
	(0.002)	(0.002)	(0.03)	(0.33)	(130)	(10)	(0.14)	(2.4)	(2.3)	(430)
145	3.577	2.621	6.04	1.03	3281	210	12.38	211.7	187.9	3257
	(0.002)	(0.003)	(0.03)	(0.79)	(375)	(10)	(0.15)	(2.5)	(2.6)	(445)
146	3.587	2.562	6.36	1.19	3663	200	12.68	202.0	203.1	3667
	(0.002)	(0.004)	(0.03)	(0.69)	(395)	(10)	(0.15)	(2.5)	(2.8)	(495)

† – measurement uncertainty, ρ – STP bulk density, d – sample thickness, v_{imp} – impact velocity, $\hat{\epsilon}_{exp}$ – experimentally-constrained greybody effective emissivity, T_{exp} – experimentally-constrained greybody absolute temperature, t_r – time during radiation history used when Imod constraining T_{exp} and $\hat{\epsilon}_{exp}$ was read, U – calculated shock wave velocity, t_{st} – calculated transit time of shock wave through MgO, P_{MgO} – calculated pressure of shock-compressed state of MgO, T_{MgO} – calculated temperature shock-compressed state of MgO.

we choose as representative of the other estimates, within experimental uncertainties. The average uncertainty of T_{MgO} is somewhat higher than, but relatively close to, the average experimental uncertainty of $T_{exp}(t_r)$. Note that the calculated shock-wave transit times through MgO are, on average, about 40 ns less than the duration of each experiment, as defined by a break in the radiation history about 240 ns after the rise in radiation intensity (see Figs 2 and 3, and compare with t_{st} for shot 146 in Table 6) due to release of MgO. This seems to be a real discrepancy; experimental times should be resolvable to within ±5 ns. We have no explanation at this point.

The good agreement between the temperatures inferred from the radiation data and calculation using (8) implies *a posteriori* that the assumptions of (i) MgO compresses as an elastic fluid, (ii) MgO does not change phase during shock compression, and (iii) $c_v = 3nR/M$ for MgO, are valid for the range of pressures covered by our experiments. The first

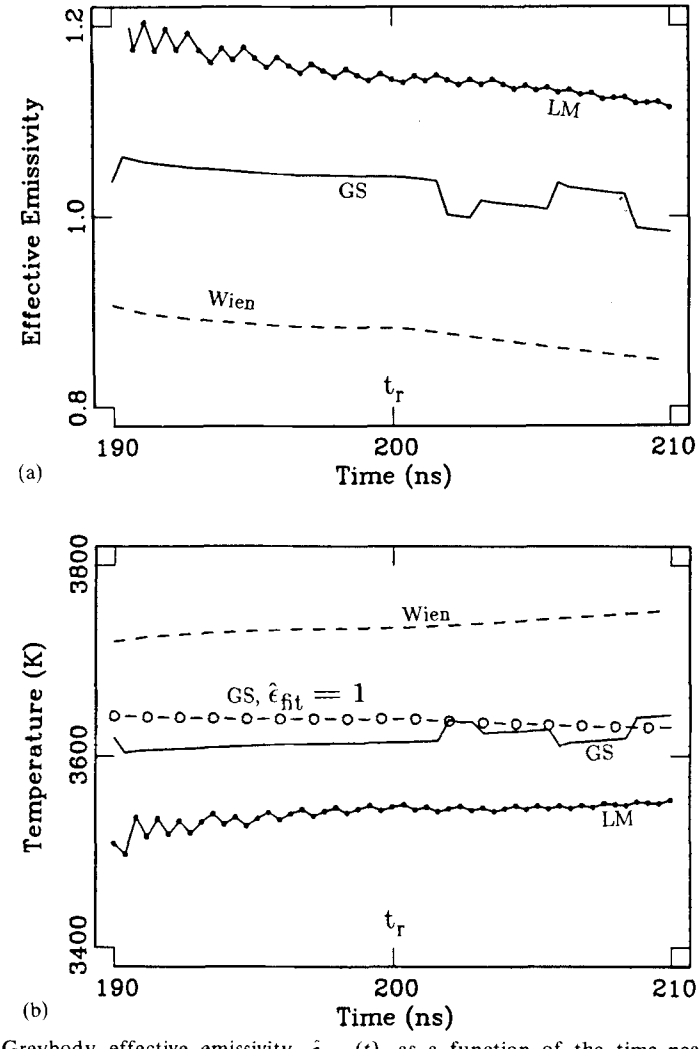

Figure 8. (a) Greybody effective emissivity, $\hat{\epsilon}_{exp}(t)$, as a function of the time near the end of the radiation history of shot 146. The fits are essentially time-independent in this time window centred on t_r. (b) Greybody absolute temperature, $T_{exp}(t)$, as a function of time and wavelength near the end of the radiation history of shot 146.

assumption implies that the temperatures achieved by MgO during shock compression in the pressure range covered are governed by its bulk elastic properties and lattice specific heat. At much lower pressures ($\lesssim 60$ GPa), MgO radiates nonthermally (Schmitt & Ahrens 1984), which is also consistent with these calculations; T_{MgO} in this pressure range is $\lesssim 500$ K.

No variation of c_v and/or γ is reflected in the uncertainties for T_{MgO} listed in Table 6. Any variation of these parameters would, of course, only increase the uncertainty of T_{MgO}, which already encompasses that of $T_{exp}(t_r)$. In other words, unless we 'assume' that we can actually calculate T_{MgO} much better than indicated by its uncertainties listed in Table 6, $T_{exp}(t_r)$ cannot place bounds on a possible variation of c_v or γ, because the uncertainty of T_{MgO} is larger than that of $T_{exp}(t_r)$. With this in mind, we can alter the values of c_v and γ given in Table 1 and obtain other values for T_{MgO} than those given in Tables 2 and 6. As discussed above, T_{MgO} is much more sensitive to variations in c_v than γ. For example, using the conditions of shot 146, if we first vary γ_0, and then $c_v = 3nR/M$, of MgO (Table 1) by ±10 per cent, we get a ±20 and ±350 K variation in T_{MgO}, respectively.

We display the experimental results in Fig. 8 along with temperatures inferred from radiation data for SiO_2 (Lyzenga *et al.* 1983) and Mg_2SiO_4 (Lyzenga & Ahrens 1980). The continuous curve is the calculated locus of shock-compressed states for MgO, and the dot-dashed curve is a Lindemann estimate of the melting curve of MgO, calculated from the parameters listed in Table 1 by estimating the compression of solid-MgO along the melting curve from the MgO shock-compression curve at the same pressure (Svendsen *et al.* 1987). Also displayed are the mantle temperature profiles of Brown & Shankland (1980) and

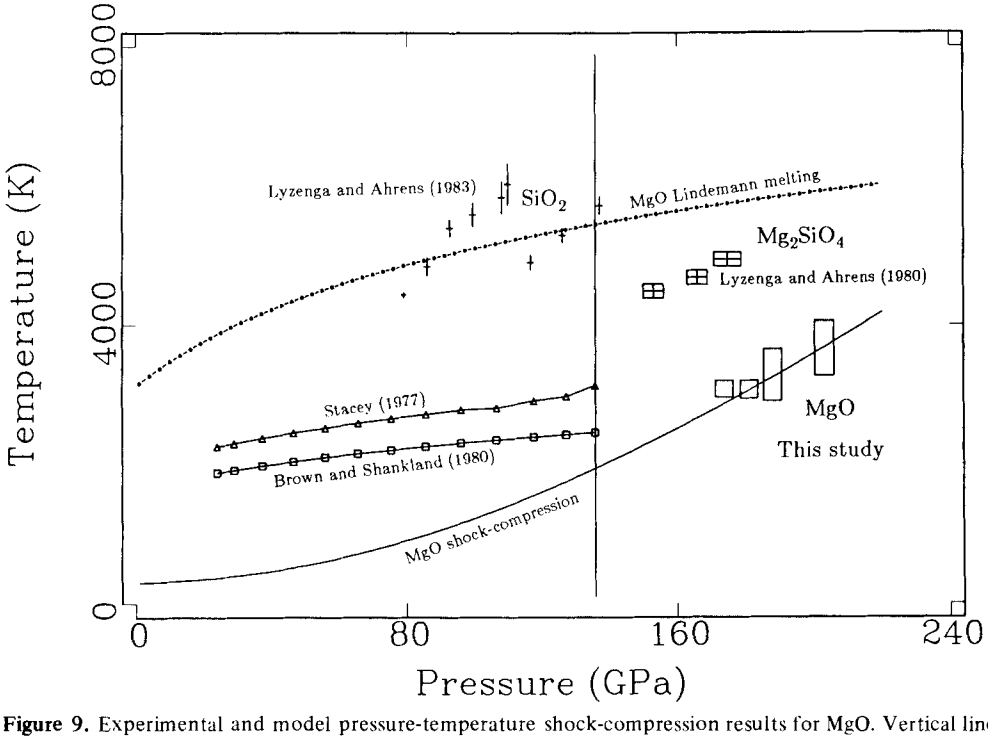

Figure 9. Experimental and model pressure-temperature shock-compression results for MgO. Vertical line at 132 GPa represents pressure of the mantle–core interface for the Earth. The Lindemann melting and shock-compression curves for MgO are calculated from the parameters for MgO in Table 1. The MgO experimental results are represented by rectangles. Also shown are the mantle temperature profiles of Stacey (1977) and Brown & Shankland (1980), as well as the experimental results of Lyzenga *et al.* (1982) for SiO_2 and Lyzenga & Ahrens (1980) for Mg_2SiO_4. Note that the MgO experimental results are quite consistent with the model curve and well-below the Lindemann estimate.

Stacey (1977), which are together representative of the range of models currently considered plausible. From the agreement of data and calculations, and in light of the Lindemann estimate, we conclude that MgO does not change phase below 200 GPa. Not shown in Fig. 8 is the intersection of the model shock-compression and Lindemann curves for MgO at 265 GPa. On the basis of the 'ideal' behaviour exhibited by MgO up to this point, we speculate that it won't melt below ≈ 265 GPa. Also, if MgO has an effective emissivity near unity between 170 and 200 GPa, as our results suggest, then the observations of Kondo & Ahrens (1983) and Schmitt & Ahrens (1984), as well as the models of Svendsen & Ahrens (1986), imply that MgO probably does not localize thermal energy below this pressure. Any localization should catalyse melting or other energetically-favoured transitions at higher pressures. Shock-induced deformation in MgO is localized (Chen *et al.* 1975) in the form of microfracturing up to 60 GPa, but apparently this has no impact on the temperature field, in contrast to other oxides such as SiO_2 (Schmitt & Ahrens 1984). Apparently the energy dissipated in localized deformation in shocked-MgO is efficiently transported away before an energy density sufficient to effect melting or solid–solid transformation is attained (Svendsen & Ahrens 1986).

What are the processes responsible for the transition of MgO from predominantly a non-thermal to a thermal radiator (with $\epsilon \rightarrow 1$) between 60 and 170 GPa? The apparent change in electrical resistivity of shocked-MgO from $\gtrsim 10^3$ to $\sim 10\ \Omega \cdot$m above 92 GPa (Ahrens 1966) is consistent with either (1) close of the valence-conduction electron band-gap, or (2) proliferation of initially-present or shock-induced (Gager, Klein & Jones 1964) defects possessing free electrons. However, since the MgO band-gap appears to increase in the pressure range of our experiments (Liberman 1978; Bukowinski 1980; Chang & Cohen 1984), we speculate that, at high pressures above ~ 100 GPa, defects in thermal equilibrium with MgO are responsible for the observed radiation from MgO.

Summary

We use a model of conductive and radiative transport among the target components of our experiments to interpret the radiation history of the target in terms of its optical and thermal properties, and infer the shock-compressed temperature of MgO. On this basis, we have the following results:

(i) The model for conduction between the Ta driver, Ag film and MgO implies that the Ag–MgO interface temperature, $T_{INT}(t)$, will be approximately constant on the time scale of the radiation observations (~ 200 ns) for values of non-dimensional interface thickness ξ less than 0.1 (Ag-film thickness $\delta \lesssim 1000$ nm) or greater than 1.0 ($\delta > 10\ \mu$m). Estimates of this thickness for the Ag film of each experiment imply that $\xi < 0.1$ for all experiments. The model implies that $T_{INT}(t)$ cannot decrease by more than about 200 K in any of the experiments (regardless of the value of ξ) because of the large thermal-inertia mismatch between Ag and MgO.

(ii) Assuming $T_{INT}(t)$ is independent of time, a fit of the radiative-transport model to MgO radiation-history data implies that shocked MgO is ~ 100 times more absorbing ($a_{\lambda MgO} \sim 6300$, 7500, 4200 and 3800 m^{-1} at 450, 600, 750 and 900 nm, respectively, at 203 GPa) than unshocked MgO in the pressure range covered by the experiments. The coefficient of absorption for shocked MgO and the effective normal spectral reflectivity of the shock-front and Ag–MgO interface wavelength-dependent in this fit (Table 4). Also, T_{INT} from this fit is much higher ($\sim 20\,000$ K) than estimated from ideal-release calculations for solid Ag-film, implying that the Ag film may be slightly porous ($\lesssim 10$ per cent) and/or reshocked. Independent constraints on $T_{INT}(t)$ and $\hat{\epsilon}_{\lambda INT}(t)$ through

modification of the experiment to record both interface and sample radiation intensities are needed to pin these possibilities down.

(iii) The radiative transport model fits imply that greybody fits to the end of the radiation histories for each experiment constrain the effective normal (wavelength-averaged) emissivity and absolute temperature of MgO. Using two different fitting techniques, we establish, within experimental uncertainty, the robustness of our fits. The greybody fits agree well with model temperature calculations, implying that, between 170 and 200 GPa, MgO compresses as an elastic fluid with a Dulong–Petit specific-heat value. The agreement between $T_{exp}(t_r)$ and T_{MgO}, the latter calculated assuming no phase transformations, as well as the values of $\hat{\epsilon}_{exp}(t_r)$ ($\sim$0.1–1.0, Table 5), together imply that MgO does not change phase below 200 GPa. In addition, since the calculated shock-compression curve and Lindemann melting curve of MgO intersect at 265 GPa, we speculate that it will not melt below this pressure.

(iv) Comparison of the experimental results for MgO with those of SiO_2 and Mg_2SiO_4 show that the shock-compressed temperatures of Mg_2SiO_4 lie between those of SiO_2 (below) and MgO (above), analogous to the density-pressure relations between these materials, and emphasizing the role of the bulk elastic properties of these materials in controlling the first-order magnitude of their respective shock-compressed temperatures. Comparison of the extrapolated MgO shock-compression curve with a range of possible mantle temperature profiles implies that shocked MgO is colder than the lower mantle by $\sim$1000–1500 K at the same pressure.

Acknowledgments

We thank Papo Gelle, Mike Long, Chuck Manning and Leon Young for experimental assistance, Gregory Miller, Jay D. Bass, Douglas R. Schmitt and James A. Tyburczy provided enlightening discussions. We also thank Mark B. Boslough and an anonymous reviewer for constructive comments on the first draft of this paper. Support from NSF grant EAR-8608249 is gratefully acknowledged. Contribution 4413, Division of Geological and Planetary Sciences, California Institute of Technology, Pasadena, California.

References

Ahrens, T. J., 1966. High-pressure electrical behaviour and equation of state of magnesium oxide from shock wave measurements, *J. appl. Phys.*, **37**, 2532–2541.

Ahrens, T. J., Anderson, D. L. & Ringwood, A. E., 1969. Equation of state and crystal structure of high-pressure phases of shocked silicates and oxides, *Rev. Geophys.*, **7**, 667–707.

Alers, G. A., 1965. Use of sound velocity measurements in determining the Debye temperature of solids, in *Physical Acoustics*, **3B**, pp. 1–42, ed. Mason, W. P., Academic Press, New York.

Bass, J. D., Svendsen, B. & Ahrens, T. J., 1987. The temperatures of shock-compressed iron, in *High Pressure Research in Geophysics and Geochemistry*, eds. Manghnani, M. & Syono, Y., American Geophysical Union, in press.

Berman, R., 1976. *Thermal Conduction in Solids*, Oxford University Press.

Boslough, M. B., 1984. Shock-wave properties and high-pressure equations-of-state of geophysically-important materials, *PhD dissertation*, California Institute of Technology, Pasadena, California.

Boslough, M. B., 1985. A model for time dependence of shock-induced thermal radiation of light, *J. appl. Phys.*, **56**, 3394–3399.

Boslough, M. B., Ahrens, T. J. & Mitchell, A. C., 1984. Shock temperatures in CaO, *J. geophys. Res.*, **89**, 7845–7851.

Boslough, M. B., Ahrens, T. J. & Mitchell, A. C., 1986. Shock temperatures in anorthite glass, *Geophys. J. R. astr. Soc.*, **84**, 475–489.

Bridgman, P. W., 1952. The resistance of 72 elements, alloys and compounds to 100,000 kg/cm^2, *Proc. Am. Acad. Arts Sci.*, **81**, 167–251.

Brown, J. M. & Shankland, T., 1980. Thermodynamic parameters of the Earth as determined from seismic profiles, *Geophys. J. R. astr. Soc.*, **66**, 579–596.

Brown, J. M. & Shaner, J. W., 1984. Rarefaction velocities in shocked tantalum and the high pressure melting point, in *Shock Waves in Condensed Matter – 1983*, pp. 91–94, eds Asay, J. R., Graham, R. A. & Straub, G. K., Elsevier, Amsterdam.

Bukowinski, M., 1980. Pressure bonding in MgO, *J. geophys. Res.*, **85**, 285–292.

Carslaw, H. S. & Jaeger, J. C., 1959. *Conduction of Heat in Solids*, Clarendon Press, Oxford.

Carter, W. J., Marsh, S. P., Fritz, J. N. & McQueen, R. G., 1971. The equation of state of selected materials for high-pressure references, in *Accurate Characterization of the High-Pressure Environment*, pp. 147–158, NBS Special Publication 326.

Chang, K. J. & M. L. Cohen, 1984. High-pressure behavior of MgO: Structural and electronic processes, *Phys. Rev. B*, **30**, 4774–4780.

Chen, Y., Abraham, M. M., Turner, T. J. & Nelson, C. M., 1975. Luminescence in deformed MgO, CaO and SrO, *Phil. Mag.*, **32**, 99–112.

Davies, G. F., 1973. Quasi-harmonic finite strain equations-of-state of solids, *J. Phys. Chem. Solids*, **34**, 1417–1429.

Dick, J. J. & Styris, D. L., 1975. Electrical resistivity of silver foils under uniaxial shock-wave compression, *J. Appl. Phys.*, **46**, 1602–1617.

Gaffney, E. S. & Ahrens, T. J., 1973. Optical absorption spectra of ruby and periclase at high shock pressure, *J. geophys. Res.*, **78**, 5942–5953.

Gager, W. B., Klein, M. J. & Jones, W. H., 1964. The generation of vacancies in MgO single crystals by explosive shock, *Apply. Phys. Lett.*, **5**, 130–131.

Grover, R. & Urtiew, P. A., 1974. Thermal relaxation at interfaces following shock compression, *J. appl. Phys.*, **45**, 146–152.

Jackson, I. & Ringwood, A. E., 1981. High-pressure polymorphism of the iron oxides, *Geophys. J. R. astr. Soc.*, **64**, 767–783.

Jackson, I. & Niesler, H., 1982. The elasticity of periclase to 3 GPa and some geophysical implications, in *High-Pressure Research in Geophysics* (*Adv. Earth Planet. Sci. 12*), pp. 93–113, eds Akimoto, S. & Manghnani, M. H., Reidel, Dordrecht.

Jeanloz, R. & Ahrens, T. J., 1980a. Equations of state of FeO and CaO, *Geophys. J. R. astr. Soc.*, **62**, 505–528.

Jeanloz, R. & Ahrens, T. J., 1980b. Anorthite: thermal equation of state to high pressures, *Geophys. J. R. astr. Soc.*, **62**, 529–549.

Jeanloz, R., Ahrens, T. J., Mao, H. K. & Bell, P. M., 1980. B1–B2 transition in calcium oxide from shock-wave and diamond cell experiments, *Science*, **206**, 829–830.

Jeanloz, R. & Thompson, A. B., 1983. Phase transitions and mantle discontinuities, *Rev. Geophys. Space Phys.*, **21**, 51–74.

Keeler, R. N., 1971. Electrical conductivity of condensed media at high pressures, in *Physics of High Energy Density. Proc. Enrico Fermi Int. Sch. Phys.*, Course **XLVII**, 106–124, Academic Press, New York.

Kieffer, S. W., 1979. Thermodynamics and lattice vibrations of minerals: 3. Lattice dynamics and an approximation for minerals with application to simple substances and framework silicates, *Rev. Geophys. Space Phys.*, **17**, 35–59.

Knittle, E. & Jeanloz, R., 1986. High-pressure metallization of FeO and implications for the Earth's core, *Geophys. Res. Lett.*, **13**, 1541–1544.

Kondou, K. E. & Ahrens, T. J., 1983. Heterogeneous shock-induced thermal radiation in minerals, *Phys. Chem. Minerals*, **9**, 173–181.

Kormer, S. B., 1968. Optical study of the characteristics of shock-compressed condensed dielectrics, *Sov. Phys. Uspekhi*, **11**, 229–254.

Kormer, S. B., Sinitsyn, M. V., Kirillov, G. A. & Popova, L. T., 1966. An experimental determination of the light absorption coefficient in shock-compressed NaCl. The absorption and conductivity mechanism, *Sov. Phys.-JETP*, **22**, 97–105.

Liberman, D. A., 1978. Self-consistent field electronic structure calculations for compressed magnesium oxide, *J. Phys. Chem. Solids*, **39**, 255–257.

Lyzenga, G. A., 1980. Shock temperatures of materials: experiments and applications to the high pressure equation of state, *PhD dissertation*, California Institute of Technology, Pasadena, California.

Lyzenga, G. A. & Ahrens, T. J., 1978. The relation between the shock-induced free-surface velocity and the postshock specific volume of solids, *J. appl. Phys.*, **49**, 201–204.

Lyzenga, G. A. & Ahrens, T. J., 1980. Shock temperature measurements in Mg_2SiO_4 and SiO_4 at high pressures, *Geophys. Res. Lett.*, 7, 141–144.

Lyzenga, G. A., Ahrens, T. J. & Mitchell, A. C., 1983. Shock temperatures of SiO_2 and their geophysical implications, *J. geophys. Res.*, 88, 2431–2444.

Marsh, S. P., 1980. *LASL shock Hugoniot data*, University of California Press, Los Angeles, CA.

Mitchell, A. C. & Nellis, W. J., 1981. Shock compression of aluminium, copper and tantalum, *J. appl. Phys.*, **52**, 3363–3374.

Press, W. H., Flannery, B. P., Teukolsky, S. A. & Vetterling, W. T., 1986. *Numerical Recipes: The Art of Scientific Computing*, Cambridge University Press, New York.

Rice, W. H., McQueen, R. G. & Walsh, J. M., 1958. Compressibility of solids by strong shock waves, *Solid State Phys.*, 6, 1–63.

Robie, R. A., Hemingway, B. S. & Fisher, R. J., 1978. *Thermodynamic properties of minerals and related substances at 298.15 K and 1 bar (10^5 Pascals) pressure and at higher temperatures*, USGS Bulletin 1452, Government Printing Office, Washington, D.C.

Roufosse, M. C. & Klemens, P. G., 1974. Lattice thermal conductivity of minerals at high temperature, *J. geophys. Res.*, 79, 703–705.

Schmitt, D. R. & Ahrens, T. J., 1984. Emission of shock compressed solids, in *Shock waves in Condensed matter – 1983*, pp. 313–316, eds Asay, J. R., Graham, R. A. & Straub, G. K., Elsevier.

Schmitt, D. R., Svendsen, B. & Ahrens, T. J., 1986. Shock-induced radiation from minerals, in *Shock Waves in Condensed Matter – 1985*, pp. 262–266, ed. Gupta, Y. M., Plenum Press, New York.

Schneider, H. & Jung, I., 1982. Structural deformation of experimentally shock-loaded periclase (MgO), *Phil Mag.*, 27, 140–144.

Siegel, R. & Howell, J. R., 1980. *Thermal Radiation Heat Transfer*, McGraw-Hill, New York.

Stacey, F., 1977. A thermal model of the Earth, *Phys. Earth planet. Int.*, 15, 341–348.

Svendsen, B., 1987. Optical radiation from shock-compressed materials, *PhD dissertation*, California Institute of Technology.

Svendsen, B. & Ahrens, T. J., 1986. Thermal history of shock-compressed solids, in *Shock Waves in Condensed Matter – 1985*, pp. 607–613, ed. Gupta, Y. M., Plenum Press, New York.

Svendsen, B., Bass, J. D. & Ahrens, T. J., 1987. Optical radiation from shock-compressed interfaces and materials, in *High Pressure Research in Geophysics and Geochemistry*, eds Manghnani, M. H. & Syono, Y., American Geophysical Union, in press.

Svet, D. I., 1965. *Thermal Radiation: Metals, Semiconductors, Ceramics, Partly Transparent Bodies, and Films*, Consultants Bureau, Plenum Press, New York.

Touloukian, Y. S., Powell, R. W., Ho, C. Y. & Klemens, P. G., 1970a. *Thermo-physical Properties of Matter, Volume 1: Thermal Conductivity*, Thermophysical Properties Research Center of Purdue University, Data Series, Plenum Press, New York.

Touloukian, Y. S., Powell, R. W., Ho, C. Y. & Klemens, P. G., 1970b. *Thermo-physical Properties of Matter, Volume 7: Thermal Radiative Properties, metallic elements and alloys*, Thermophysical Properties Research Center of Purdue University, Data Series, Plenum Publishing Corporation, New York.

Touloukian, Y. S., Powell, R. W., Ho, C. Y. & Klemens, P. G., 1970c. *Thermo-physical Properties of Matter, Volume 8: Thermal Radiative Properties, non-metallic solids*, Thermophysical Properties Research Center of Purdue University, Data Sereis, Plenum Press, New York.

Touloukian, Y. S., Powell, R. W., Ho, C. Y. & Klemens, P. G., 1975. *Thermophysical Properties of Matter, Volume 12: Thermal expansion*, Thermophysical Properties Research Center of Purdue University, Data series, Plenum Press, New York.

Urtiew, P. A., 1974. Effect of shock loading on transparency of sapphire crystals, *J. appl. Phys.*, **45**, 3490–3493.

Urtiew, P. A. & Grover, R., 1974. Temperature deposition caused by shock interactions with material interfaces, *J. appl. Phys.*, **45**, 140–145.

Vassioliou & Ahrens, 1981. Hugoniot equation of state of periclase to 200 GPa, *Geophys. Res. Lett.*, **8**, 729–732.

Vedam, K. & Schmidt, E. D. D., 1966. Variation of refractive index of MgO with pressure to 7 kbar, *Phys. Res.*, **146**, 548–554.

Weast, R. C., ed., 1979. *CRC Handbook of Chemistry and Physics*, 60th edition, CRC Press.